Revisiting Solidification Microstructure Selection Maps in the Frame of Additive Manufacturing

P. Mohammadpour[a], A. Plotkowski[b,c], A.B. Phillion[a,*]

[a] *Department of Materials Science and Engineering, McMaster University, Hamilton, Canada*
[b] *Materials Science and Technology Division, Oak Ridge National Laboratory, Oak Ridge, TN, USA*
[c] *Manufacturing Demonstration Facility, Oak Ridge National Laboratory, Knoxville, TN, USA*

Abstract

Understanding microstructural development in additive manufacturing under highly non-equilibrium cooling conditions and the consequent effects on mechanical properties of the final component is critical for accelerating industrial adoption of these manufacturing techniques. In this study, simple but effective theoretical solidification models are recalled to evaluate their ability to predict of microstructural features in additive manufacturing applications. As a case study, the resulting solidification microstructure selection maps are created to predict the stable growth modality and the columnar to equiaxed transition (CET) of an Al-10Si-0.5Mg alloy processed via selective laser melting. The potential of this method in microstructural predictions for additively manufactured products, as well as outstanding challenges and limitations, are discussed.

Keywords: Rapid solidification; Solidification microstructure selection maps; Additive manufacturing; Columnar to equiaxed transition

1. Introduction

Metal-based additive manufacturing (AM) promises a great ability to produce complex geometries, and reduced lead times by eliminating expensive downstream processing stages [1]. However, there are a number of significant challenges that must be overcome for this set of techniques to reach wide industrial adoption. In metal AM, the process of part consolidation begins via laser, electron beam, or arc melting. The resulting non-equilibrium solidification conditions lead to a variety of microstructures - often preferentially selecting non-equilibrium growth modes or displaying variations in columnar or equiaxed

*Corresponding author
Email address: andre.phillion@mcmaster.ca (A.B. Phillion)

grain morphologies [2, 3, 4], which consequently result in a wide range of mechanical properties. The microstructure achieved during solidification is a result of the melt thermal conditions, alloy chemistry, and thermodynamic properties. Understanding these phenomena will aid in reducing unwanted variability in material properties and even enable the design of site-specific microstructural features to suit a given application.

About 30 years ago, Kurz, Trivedi, and colleagues proposed a set of analytical models that describe the growth of planar [5], dendritic (KGT model [6]), eutectic (TKM model [7]), and banded [8] microstructures during rapid unidirectional solidification. Concurrently, Hunt proposed an analytical model [9], later extended by Gaumann et al. [10], to identify the thermal conditions required to transition from columnar to equiaxed grain morphologies. Collectively, these analytical expressions can be used to create Solidification Microstructure Selection (SMS) maps, *i.e.* to predict the solidification microstructure and grain morphology that forms for a set of alloy composition and thermal conditions. A tool that efficiently maps the structure - process relationship would be very informative in guiding AM development.

The creation of SMS maps is computationally efficient when compared to more complex approaches such as phase field and cellular automata and has been used to predict microstructure during laser treatment processes [11, 12, 13, 14, 15], among others. Although solidification during AM is not unidirectional at the scale of the melt pool, the assumption of local unidirectional solidification at the scale of the dendrite tips is required in order to create SMS maps using the provided analytical expressions. Recently, Kurz and Trivedi's expressions have been used to create SMS maps for an Al-12%Ce alloy to validate the suitability of this alloy for AM applications [16, 17]. Although only limited thermodynamic data was available for the Al-Ce system, the authors predicted reasonably well the developed microstructure when compared against experimental data for different thermal conditions. Further, variations on Hunt's expression has been used by a number of authors to predict whether columnar or equiaxed microstructures form during metal AM [18, 19, 20, 21, 22, 2].

In this study, we revisit the above analytical expressions required to create SMS maps in the context of Selective Laser Melting (SLM), a powder-bed metal AM process. The main advantages of analytical expressions is their high-throughput and simple extension to multi-component systems. Although accuracy is sacrificed, SMS maps provide the opportunity to efficiently assess a wide parameter space and to act as a guide for more detailed numerical simulations. This work provides a detailed yet concise presentation of the equations, assumptions, and limitations of the different models so that future researchers can fully utilize the SMS approach to improve the properties of SLM -produced components. As a case study, these models are applied to the Al-Si-Mg ternary system. This system is the current standard for AM of Al alloys and has readily available thermodynamic data.

2. Growth Models for Solidification Microstrutures

Interface response, i.e. the solid/liquid interface temperature of a specific solidification mode as a function of interface growth velocity, V for a given alloy composition, C_0 and thermal gradient, G form the basis of Kurz and Trivedi's analytical models for predicting solidification microstructure under the non-equilibrium solidification conditions. The set of solidification modes to be considered depends on the alloy system. For a simple binary eutectic phase diagram, four possible microstructures exist: planar, dendritic, eutectic, and banded, irrespective of the actual alloy content. The microstructure having the maximum interface temperature is the one that is most stable [12].

The underlying assumption of the theoretical equations used to predict the interface responses is columnar (directional) and steady-state growth conditions on the scale of the transport phenomena that control microstructure selection. With respect to AM, on one hand the thermal behaviour in the melt pool is highly transient and may vary by many orders of magnitude. One the other hand, the analytical models are applied on the length scale of the transport phenomena (e.g. solute diffusion at the length scale of the dendrite tip) which are indeed quite short. Although additional research is required to properly quantify the limits of this assumption, it is reasonable at present to assume that this methodology can be used to rationalize microstructure trends during AM.

2.1. Planar Growth

Assuming linear superposition of the effects of various solute elements, the interface response for planar morphology can be written as

$$T_{PL} = T_m - \sum^{i} C_{0,i} \frac{m_i^v}{k_i^v} - \frac{V}{\mu_{k,i}}, \tag{1}$$

where T_{PL} is the temperature at the planar interface, T_m is the melting point of the pure metal, the summation symbol along with the subscript i allow for generalization to multi-component systems, $C_{0,i}$ is the initial composition, m_i^v, k_i^v, and $\mu_{k,i}$ are the liquidus slope, partition coefficient and interface kinetic coefficient for each element, and V is the interface velocity. The superscript v is added to both m_i and k_i to denote the velocity-dependency because of the non-equilibrium state of the interface. This is needed to predict solidification morphologies under the complex non-equilibrium conditions found in SLM. Note that a convention of defining the liquidus slopes and all compositional gradients as positive values is adopted.

The velocity-dependent liquidus slope and partition coefficient can be defined as [23, 24]

$$m_i^v = m_i \left(1 + \frac{k_i - k_i^v[1 - \ln(k_i^v/k_i)]}{1 - k_i} \right), \text{and} \tag{2}$$

$$k_i^v = \frac{(k_i + Pe_i)}{(1 + Pe_i)}, \tag{3}$$

where m_i and k_i are the equilibrium liquidus slope and partition coefficient for each element assuming a linearized phase diagram, and Pe_i is the interfacial Péclet number for solute redistribution. Often, phase diagrams are not linear; this assumption is an important limitation of current growth models for accurately predicting microstructure. Furthermore, $\mu_{k,i}$ is approximated as

$$\mu_{k,i} \approx \frac{V_0(1 - k_i)}{m_i}, \tag{4}$$

in which V_0 is the speed of sound in the pure metal in the solid state, and Pe_i is given by

$$Pe_i = \frac{a_0 V}{D}, \tag{5}$$

where a_0 is the thickness of the diffuse layer at the solid-liquid interface and D is the solute diffusion coefficient in the liquid. D is assumed to be the same for all alloying elements while diffusion in the solid state is assumed to be negligible.

2.2. Dendritic Growth

The KGT [6] model and later work by Trivedi and Kurz [25] have been used for several years to calculate dendritic growth under rapid solidification conditions. Following their research, the non-equilibrium dendrite tip undercooling, ΔT_{tip}, can be written as

$$\Delta T_{tip} = \sum^{i} \Big(\frac{k_i^v \Delta T_{0,i}^v \mathrm{Iv}(Pe_d)}{1 - (1 - k_i^v)\mathrm{Iv}(Pe_d)} + C_{0,i}(m_i - m_i^v) + \frac{V}{\mu_{k,i}} \Big) + \frac{2\Gamma}{R} + \frac{GD}{V}, \tag{6}$$

where ΔT_0^v is the non-equilibrium solidification interval, Iv is the Ivantsov function, Γ is the Gibbs-Thomson coefficient, and Pe_d is the solutal Péclet number. The first four terms on the right-hand side represent the effects of the growth dynamics / non-equilibrium state, solute, kinetic attachment, and dendrite curvature on the dendrite tip undercooling for each solute element. The last term is related to cellular growth at low interface velocities. Although not strictly required for studies of AM, it is included for completeness.

The non-equilibrium solidification interval, which is obtained from thermodynamic considerations, is given by

$$\Delta T_{0,i}^v = \frac{m_i^v C_0 (k_i^v - 1)}{k_i^v}. \tag{7}$$

The Iv function, for different morphologies of the dendrite [25, 26], is given by

$$\begin{cases} \mathrm{Iv}(Pe_d) = Pe_d \exp(Pe_d)\mathrm{E}_1(Pe_d), & \text{needle} \\ \mathrm{Iv}(Pe_d) = (\pi Pe_d)^{1/2} \quad Pe_d \ll 1 & \text{plate} \\ \mathrm{Iv}(Pe_d) = 1 - \frac{1}{2Pe_d} + \frac{3}{4Pe_d{}^2} \quad Pe_d \gg 1 & \end{cases} \tag{8}$$

where the exponential integral function, $\mathrm{E}_1(Pe_d)$, is estimated based upon the approximation of Barry, Parlange and Li [27].

The solutal Péclet number ahead of the dendrite tip is defined as

$$Pe_d = \frac{RV}{2D}, \tag{9}$$

with the dendrite tip radius estimated from linear stability analysis [28] as

$$R = \left(\frac{\Gamma}{\sigma^* (\sum_i^i m_i G_{c,i} \xi_{d,i} - G)} \right)^{1/2}. \tag{10}$$

where σ^* is the dendrite tip selection parameter, R is the dendrite tip radius, $G_{c,i}$ is the concentration gradient in the liquid ahead of the dendrite tip, and $\xi_{d,i}$ is the deviation from the equilibrium state also known as the dendritic function of Péclet number. $\xi_{d,i}$ and $G_{c,i}$ are given by

$$\xi_{d,i} = 1 - \frac{2k_i^v}{\left[1 + \frac{1}{\sigma^* Pe_i^2}\right]^{1/2} - 1 + 2k_i^v}, \tag{11}$$

and

$$G_{c,i} = \frac{(C_{t,i} - C_{0,i})V}{D \ \mathrm{Iv}(Pe_d)}, \tag{12}$$

where $C_{t,i}$ is the dendrite tip composition,

$$C_{t,i} = \frac{C_0}{1 - (1 - k_i^v)\mathrm{Iv}(Pe_d)}. \tag{13}$$

Note that k_i^v is used in Eq. 13 instead of the equilibrium partition coefficient.

R and Pe_d are thus inter-related. Eqs. 8-13 are iteratively solved in order to determine R and Pe_d. These values are then used to calculate ΔT_{tip}. Finally, the interface temperature for dendritic morphology, T_D, can be determined,

$$T_D = T_{liq} - \Delta T_{tip}, \tag{14}$$

where T_{liq} is the equilibrium liquidus temperature.

It should be noted that the term σ^* comes from the dependence of the solute diffusion in the liquid on the Péclet number, which only gives the product of R and V and not the relationship between them. So, an additional constraint is required, specifically it is assumed that σ^* is constant for a given alloy system [25]. This assumption is valid as long as linear stability in dendritic growth remains valid [29]. It has been shown in more recent studies using phase field simulations that σ^* and thus dendritic growth directions can vary under certain conditions with alloy composition as well as imposed undercooling [30, 31]. σ^* could thus be calculated as a function of interfacial energy, alloy composition and imposed undercooling. But this is beyond the scope of the present study.

2.3. Eutectic Growth

The model of lamellar eutectic growth during rapid solidification is based on the TMK approach [7], which links the eutectic undercooling, ΔT_{eut}, to V and lamellar spacing, λ. In this model,

$$\Delta T_{eut} = K_1 \lambda V + \frac{K_2}{\lambda}, \text{and} \tag{15}$$

$$\lambda^2 \, V = \frac{K_2}{K_1}, \tag{16}$$

where K_1 and K_2 are given by velocity-dependent parameters,

$$K_1 = \sum^{i} \Big(\frac{m^v_{eut,i} C^v_{0,i}}{D} \frac{P}{f_{\alpha,i} f_{\beta,i}} \Big), \text{and} \tag{17}$$

$$K_2 = 2 \sum^{i} m^v_{eut,i} \left(\frac{\Gamma_{\alpha,i} \sin\theta_{\alpha,i}}{m^v_{\alpha,i} f_{\alpha,i}} + \frac{\Gamma_{\beta,i} \sin\theta_{\beta,i}}{m^v_{\beta,i} f_{\beta,i}} \right). \tag{18}$$

For planar and dendritic growth, the calculations are performed on a single phase; however calculations for eutectic growth must consider two phases: the solute lean α phase and the solute rich β phase. Thus $f_{j,i}$ and $\theta_{j,i}$ are the the volume fraction and contact angle of phase j for the binary system with solute i, $m^v_{j,i}$ is calculated using Eq. 2, $m^v_{eut,i}$ is the average velocity-dependent liquidus slope at the eutectic point, $C^v_{0,i}$ is the difference between the non-equilibrium composition of the two phases at the eutectic temperature, and P is an infinite series. Some of these terms require further definition. Specifically,

$$m^v_{eut,i} = \overline{m}_i \left(1 + \frac{k_i - k^v_i [1 - \ln(k^v_i / k_i)]}{1 - k_i} \right), \tag{19}$$

where $\overline{m}_i$ is the average equilibrium liquidus slope given by $\overline{m}_i = \frac{m_{\alpha,i} \cdot m_{\beta,i}}{m_{\alpha,i} + m_{\beta,i}}$,

$$C^v_{0,i} = C_{\beta,i} - k^v_{\beta,i} \Big(\frac{T_{m,i} - T_E}{m^v_{\beta,i}} \Big) - k^v_{\alpha,i} \Big(\frac{T_{m,p} - T_E}{m^v_{\alpha,i}} \Big), \tag{20}$$

where $k^v_{j,i}$ is calculated by Eq. 3, $T_{m,p}$ is the melting temperature of the pure metal, $T_{m,i}$ is the melting temperature of the second element or the intermetallic compound, and

$$P \approx 0.335 \big(f_{\alpha,i} f_{\beta,i} \big)^{1.65} \xi_{e,i}. \tag{21}$$

For eutectic growth, the solutal Péclet number, Pe_e and the eutectic function of the Péclet number, $\xi_{e,i}$, are given by

$$Pe_e = \frac{\lambda V}{2D}, \text{and} \tag{22}$$

$$\xi_{e,i} = 1 - \frac{2.5\pi / Pe_e}{\Big[1 + (\frac{2.5\pi}{Pe_e})^2 \Big]^{1/2} - 1 + 2k^v_i}. \tag{23}$$

The use of k_i^v within Eq. 23 implies that the partition coefficient of the α and β phases are equal. Either this assumption or the assumption that the α and β liquidus slopes are equal is required for the problem to be analytically tractable. A numerical model could be used to eliminate this assumption, but this would obviously be more complex and computationally expensive. Finally, the interface temperature for eutectic growth, T_E, is calculated by

$$T_E = T_{eut} - \Delta T_{eut}\,, \tag{24}$$

where T_E is the equilibrium eutectic temperature. Eqs. 15-24 are iteratively solved in order to determine T_E.

In some alloying system like Al-Si, due to the faceted interface of the Si phase, the resulting eutectic is irregular. For an irregular eutectic, the Jackson-Hunt growth model can be extended by defining a criterion to describe this microstructure in which the lamellar spacing varies. Specifically, when $\lambda = \lambda_{min}$, lamellae will stop growing and when $\lambda = \lambda_{max}$, branching will occur [28, 32]. Thus, the average spacing $\bar{\lambda}$ can be defined as

$$\bar{\lambda} = \frac{\lambda_{min} + \lambda_{max}}{2} = \varphi\lambda_{ext}\,, \tag{25}$$

where λ_{ext} is the lamellar spacing corresponding the minimum undercooling (ΔT_{eut}) at a given interface velocity and φ is a material property. The Jackson-Hunt growth kinetic model is then

$$\bar{\lambda}\Delta T_{eut} = (\varphi^2 + 1)K_2, \tag{26}$$

$$\Delta T_{eut} = (\varphi^{-1} + \varphi)\sqrt{K_1 K_2}\sqrt{V}, \text{and} \tag{27}$$

$$\bar{\lambda}^2 V = \varphi^2 \frac{K_2}{K_1}. \tag{28}$$

2.4. Banded Structure

The final probable microstructure that could form during rapid solidification occurs when solute trapping causes a loss of equilibrium in the moving interface. This interface instability results in oscillatory behaviour between the plane front and dendritic microstructures, *i.e.* a banded structure [8, 15, 33] as a result of solute trapping. Solute trapping occurs solely due to the high interface velocity and is not dependent on the thermal gradient [28, 25]. Based on a stability analysis of the interface, the banded structure will form between the range of velocities corresponding to the minimum dendritic growth interface temperature, and the maximum planar front interface temperature. This condition can be expressed as:

$$V_B^{min} : \frac{dT_D}{dV} = 0 \text{ and } \frac{dT_D^2}{dV^2} > 0, \tag{29}$$

$$V_B^{max} : \frac{dT_{PL}}{dV} = 0 \text{ and } \frac{dT_{PL}^2}{dV^2} < 0. \tag{30}$$

where V_B is the velocity of formation of the banded structure.

2.5. Grain Morphology

In both dendritic and eutectic solidification [9], one must also differentiate between columnar and equiaxed grains. Most metallic AM components show anisotropy in mechanical properties due to the favourability in forming columnar grains. For some applications this is desirable, but others require instead equiaxed grains to improve both process and product performance. In recent years there has been considerable experimental research carried out to enhance the homogeneity of AM microstructures through manipulation of G and V. Predicting the columnar-to-equiaxed transition (CET) is challenging owing to the complexity of this phenomenon. Gaumann's expression [10], building on Hunt's criterion [9], can be used to predict whether the rapidly solidified grain morphology will be columnar or equiaxed. This expression relates the volume fraction of equiaxed grains, ϕ, to G as

$$G = \frac{1}{1+n}\sqrt[3]{\frac{-4\pi N_0}{3\ln(1-\phi)}}\Delta T_c\Big(1 - \frac{\Delta T_n^{n+1}}{\Delta T^{n+1}}\Big), \tag{31}$$

where N_0 is the nucleant volume density for equiaxed grains, ΔT is the undercooling for columnar growth, ΔT_n is the nucleation undercooling for equiaxed grains, and n is a material constant. Based on several studies, a fully equiaxed microstructure is achieved with $\phi > 0.49$, while a fully columnar microstructure is achieved with $\phi < 0.0066$ [34, 21].

There are two main limitations to this approach to determining the CET. The first is the assumption of constant values for nucleant density and nucleation undercooling as these are known to be linked to alloy and nuclei composition, the presence of impurities, and the kinetics of atom attachment, and are better represented as a distribution of nucleation site characteristics [35]. A precise prediction of CET can only be obtained if the effect of these parameters on N_0 and ΔT_n are known; however, this is extremely challenging in cases where grain refiner particles are not intentionally added. Consequently, they represent a significant source of uncertainty in these CET models.

The second limitation lies within the derivation of Hunt's criterion itself, as a simplified relationship between dendrite growth velocity and undercooling that neglects the effects of thermal gradient was utilized, *i.e.* $\Delta T = \sqrt{VC_0/A}$ where A is a fitting parameter, instead of a more complex relationship such as the KGT model shown in Section 2.2. Furthermore, the same growth model was applied for both the directional growth of columnar dendrites, and non-oriented growth of equiaxed dendritic grains. The generality of the model could be improved by adopting an approach following Haines et al. [21] whereby the KGT model is used to predict undercooling for columnar dendritic, which is then substituted directly into Eq. 31. However, the equiaxed growth velocity was still calculated using a simplified relationship, and an appropriate equiaxed growth algorithm to assist CET predictions has not been determined.

3. Results and Discussion

The above set of models defines the interface temperatures of planar, dendritic, banded, and eutectic solidification microstructures, as well as the transition in grain morphology from columnar to equiaxed for a given V, G, and $C_{0,i}$. Their application requires considerable thermo-physical properties. T_m, m_i and k_i, $f_{j,i}$ can be taken from thermodynamic databases while a_0, V_0, σ^*, Γ, θ_j and D must typically be experimentally-determined, or estimated from atomistic simulations [36] and are sometimes found in the literature. All used thermophysical and thermodynamic properties are summarized in table. 1 The terms k_i^v and m_i^v can be calculated from Eqs. 2 and 3, and are assumed to be the same for all types of growth. Furthermore, it is assumed that the maximum value of the interface growth velocity, V, is maximally bounded by the scanning speed[37]. Scanning speeds in SLM typically vary between ≈0.3-1.4 m/s. The corresponding thermal gradient in the mushy zone duing SLM can be determined, as a first approximation, using the Rosenthal Equation [38]. Applying this equation to the common AM alloy Al-10wt.%Si-0.5wt.%Mg (AlSi10Mg) while assuming an energy input of $P = 200$W and a scanning speed $V = 1.4$ m/s [39], the SLM thermal gradients along the edge of the radius of the melt pool range from 10^6K/m to 10^9K/m.

Although the Rosenthal solution is a very quick way for prediction of the thermal history, due to the use of various simplifying assumptions, it gives only a rough estimation of the temperature profile. One of the most important limitations of the Rosenthal solution is the neglection of convection in the melt pool. Marangoni flow, i.e. an inevitable phenomenon resulting from a high heat input during laser heating and its influence on the local temperature dependent surface tension, may cause significant variation in the melt pool shape and resulting thermal profile. To address this limitation, future work will involve a precise thermal-flow calculation using numerical methods.

3.1. Interface Response

As shown in Fig. 1, the pseudo-binary Al-Si phase diagram with 0.5 wt% Mg - calculated via the Thermo-Calc software using the COST 507 database-, shows that the microstructure of AlSi10Mg may possibly contain α-Al (FCC), Si (Diamond cubic) and eutectic phases. The resulting possible solidification microstructure are α-Al plane front, α-Al dendritic, Si-primary, and eutectic. The Si-planar growth is neglected due to the extremely low solubility of Al in Si. Further, it is assumed that the Si-primary growth morphology is plate-like. Thus, the second Ivantsov function in Eq.8, for plates, has been used for this interface response calculation.

Fig. 2 shows the resulting set of interface responses for the possible solidification microstructures. As previously explained in Section 2, the stable solidification microstructure is the one with the highest interface temperature. For this alloy, the stable solidification microstructure changes with increasing growth velocity as: eutectic → α-Al dendritic → banded → planar. Further, as shown in the figure, the stable solidification microstructures during SLM is expected to

Table 1: Physical and thermodynamic properties of Al-Si-Mg system [13, 35, 40, 41, 42].

Parameter		**Unit**
Initial composition of Si, $C_{0,Si}$	10	wt%
Initial composition of Mg, $C_{0,Mg}$	0.5	wt%
Melting temperature of pure Al, $T_{m,Al}$	933.33	K
Melting temperature of pure Si, $T_{m,Si}$	1687	K
Eutectic composition, C_{Eut}	12.63	wt%Si
Eutectic temperature, T_{Eut}	848	K
Liquidus slope of phase α in Al-Si pseudo-binary system, $m_{\alpha,Si}$	6.74	Kwt%$^{-1}$
Liquidus slope of phase α in Al-Mg pseudo-binary system, $m_{\alpha,Mg}$	3.1	Kwt%$^{-1}$
Liquidus slope of phase Si Al-Si pseudo-binary system, m_{Si}	9.59	Kwt%$^{-1}$
Partition coefficient of phase α in Al-Si pseudo-binary system, $k_{\alpha,Si}$	0.131	-
Partition coefficient of phase α in Al-Mg pseudo-binary system, $k_{\alpha,Mg}$	0.47	-
Partition coefficient of phase Si in Al-Si pseudo-binary system, k_{Si}	5×10^{-11}	-
Gibbs-Thomson coefficient for the phase α, Γ_α	1.96×10^{-7}	mK
Gibbs-Thomson coefficient for the phase Si, Γ_{Si}	1.7×10^{-7}	mK
Contact angle of phase α, θ_α	30	degrees
Contact angle of phase Si, θ_{Si}	65	degrees
Volume fraction of phase α, f_α	0.8684	
Volume fraction of phase Si, f_{Si}	0.1316	
Diffusion coefficient in the liquid, D	3×10^{-9}	m^{2}s^{-1}
Speed of sound in pure Al, V_0	5100	ms^{-1}
Diffuse interface thickness, a_0	10^{-9}	m
Material property, φ	3.2	
Nucleation undercooling, ΔT_n	2	K
Nucleation density, N_0	5×10^{10}	m^{-3}
Material parameter, n	2.5	-
Dendrite Tip Selection Parameter, σ^*	$(2\pi)^{-2}$	-

be eutectic, α-Al dendritic, and perhaps banded. These predictions and micrographs of SLM-produced AlSi10Mg [39, 43, 44, 45] show reasonable agreement, specifically primary dendritic Al and a novel eutectic structure containing very small Si particles depending on the scanning speed. No banded structures have been reported in the literature. Matching predicted microstructures and micrographs is complicated by the fact that the prediction is limited to the melt pool scale; however, in AM the processing of subsequent layers will affect the microstructures of previous layers. Although it was assumed that interface growth velocity and scanning speed are equivalent, it will be the center of the melt pool which has the maximum growth velocity and thus the most probable location for forming a banded microstructure. Regardless of the scan pattern used in AM, the top-most region of the melt pool experiences the maximum rate of growth velocity and consequently banded microstructure. In the case that layers are subsequently printed on each other, the banded microstructure will be eliminated due to the partial melting of upper regions of those previously-processed layers. The center of the melt pool is most-likely to remelt upon processing

subsequent layers. It should also be noted that although the figure was created using $G = 10^6$K/m, simulations at higher values up to $G = 10^9$K/m showed no appreciable differences in form.

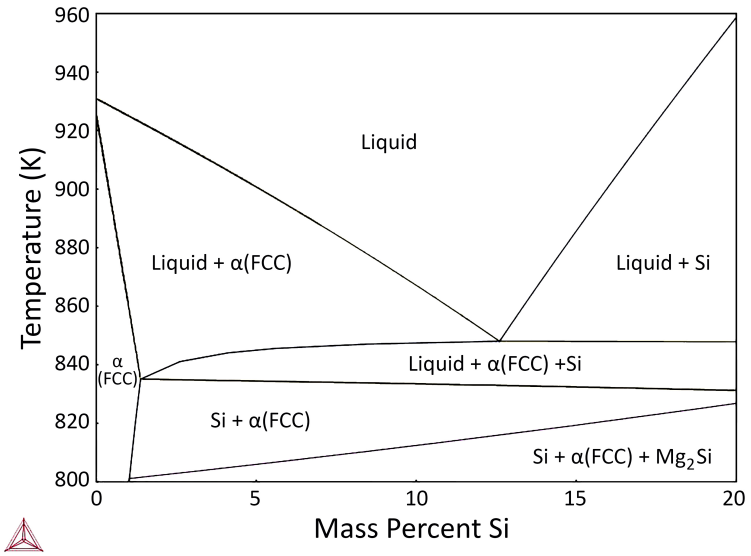

Figure 1: The pseudo-binary phase diagram of Al-Si at (0.5wt%) Mg content, calculated using Thermo-Calc Software.

3.2. SMS Maps

SMS maps are graphical representations to show the stability of microstructures under specific conditions. They are useful to track phase transformation and to design AM processes that will contain desirable mirostructures through manipulation of process parameters. Two types of SMS maps can be defined. Type 1 shows the stable solidification morphology for a set of growth velocities and alloy compositions under constant thermal gradient. Type 2 shows whether (or not) the morphology for a specific alloy composition will be expressed by columnar or equiaxed grains. Both are needed to rationalize the different kinds of microstructures achieved in AM.

A Type 1 SMS map for the Al-Si-Mg system, assuming $G = 10^6$ K/m and C_{Mg}=0.5 wt.%, is shown in Fig. 3, identifies the predominant solidification mode for a set of compositions and interface velocities. For this system at constant Mg content, the eutectic and dendritic morphologies are seen to dominate in the processing range of SLM as shown previously in Fig. 2 for the specific AlSi10Mg alloy. Type 1 SMS maps can thus be thought of as interface response diagrams extended over a range of nominal alloy compositions to show trends in solidification microstructure evolution. Although there are some dissimilarities with respect to the banded structure attributed to the layered nature of the

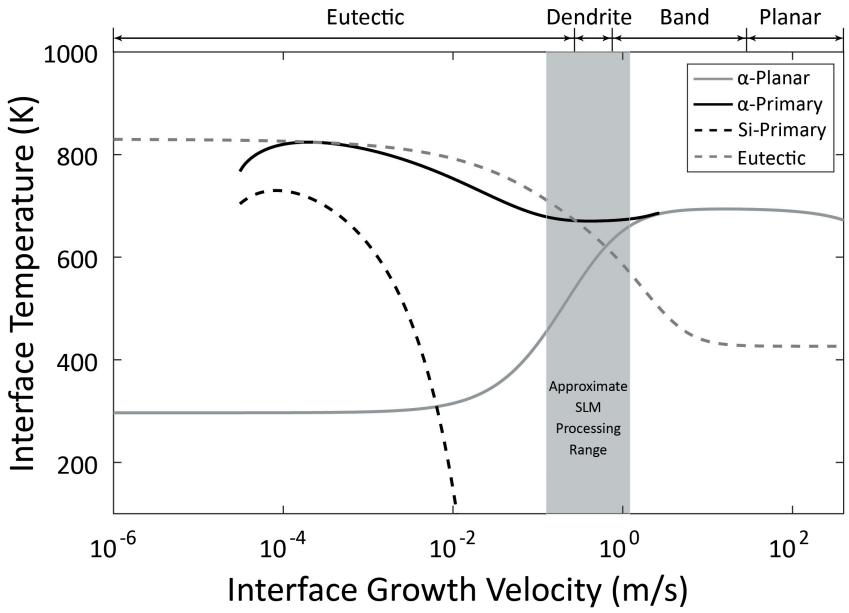

Figure 2: The variation in interface temperature with solidification velocity for all possible growth morphologies of the AlSi10Mg alloy experiencing a thermal gradient of 10^6K/m.

AM processing, such maps can be very effective in guiding SLM process and chemistry design to control solidification microstructure.

A Type 2 SMS map for the same alloy is shown in Fig. 4. This map is derived by combining the undercooling for the stable microstructure morphology predicted by the interface response with Eq.31. The nucleation density was estimated from [40, 41, 42]. Extending upon Haines's proposed approach, which utilized the undercooling from the KGT growth model to predict CET in electron beam AM [21], the term ΔT is taken as the stable value determined through the interface response analysis. Fig. 4 shows the stability range of dendritic grain morphologies for the AlSi10Mg alloy over a range of thermal gradients and interface velocities. As can be seen in the figure, the conditions present during SLM are predicted to result in both columnar dendritic and mixed equiaxed/columnar grain morphologies. Experimentally, the mixed region has been rarely found in the micrographs of SLM-produced AlSi10Mg [43, 44, 45]. It is hypothesized that this is for the same reasons as a lack of evidence for the banded structure, namely that the centre of the melt pool is likely remelted in subsequent layers. Another possible reason for a lack of experimental results showing the mixed region is that because the thermal gradients are very high, one would expect the mixed microstructure to still result in grains that compete towards columnar growth.

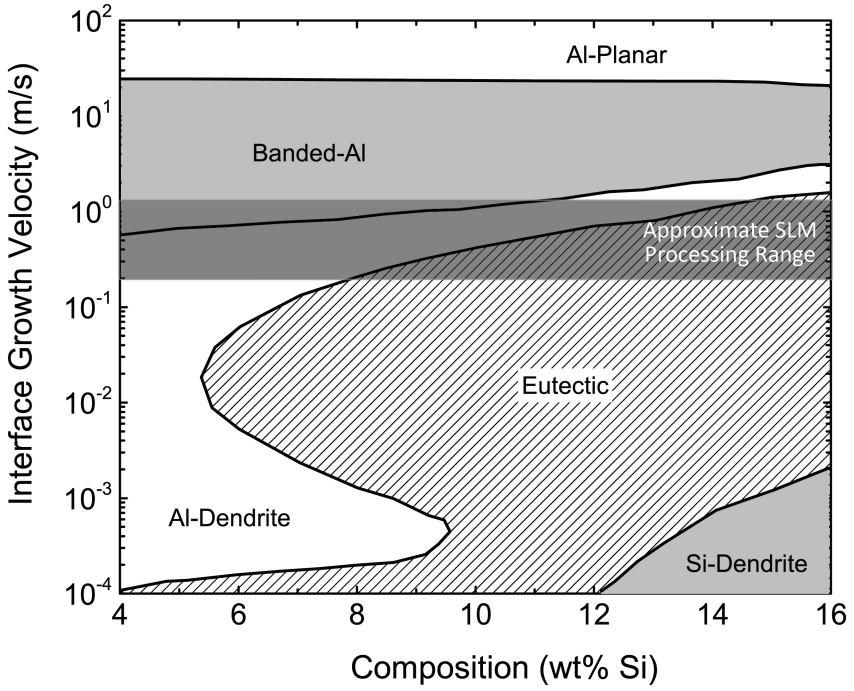

Figure 3: Type 1 SMS map for the Al-Si-Mg ternary system assuming $G = 10^6$K/m and $C_{Mg} = 0.5\%$wt.

4. Conclusions

SMS maps provide significant opportunities for improving microstructure selection during additive manufacturing. The use of analytical models that predict the interface response of the possible solidification morphologies that could exist at high thermal gradients and high solidification velocities, coupled with an analytical expression for CET will allow for new AM alloy and process development in an efficient manner, and should be used by the research community. Due to the layered nature and thermal complexity of SLM, coupling the SMS map approach with macro-scale numerical methods of heat transfer would further assist in predicting microstructure resulting from this process.

To improve the utility of SMS maps, there is need for advancement both in materials data and with respect to the method's application to additive manufacturing. Specifically, there is need to improve the availability of thermodynamic data for new alloy systems (which is also a requirement for other modeling techniques, such as phase field), develop new approaches that do not require assumptions of a linearized phase diagram and a constant dendrite tip selection parameter, and enhance the characterization method for more accurate estimation of nucleant density and equiaxed nucleation undercooling. Furthermore,

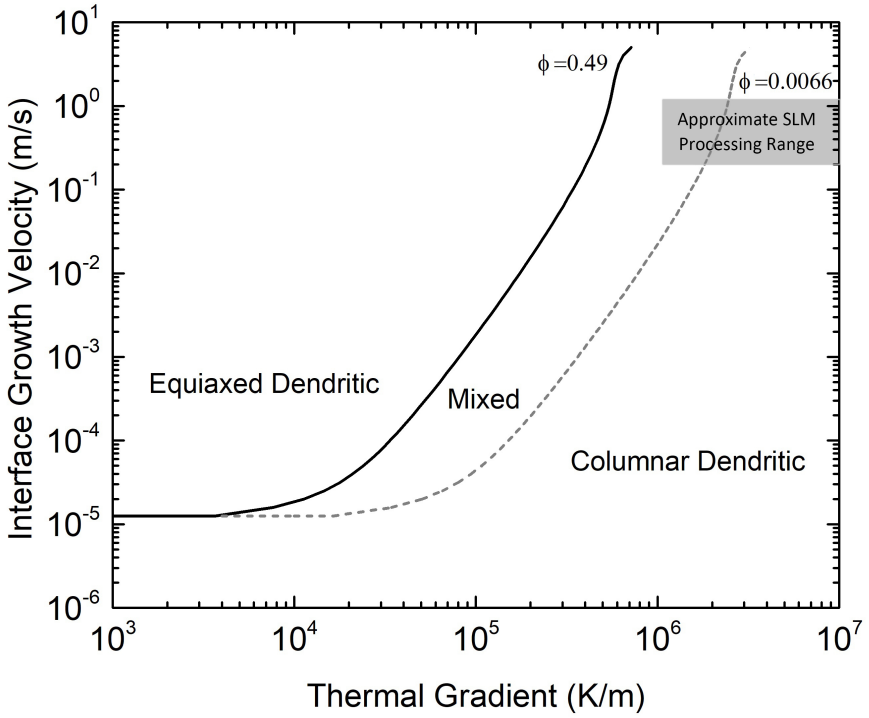

Figure 4: Type 2 SMS map for the a Al-10wt.%Si-0.5wt.%Mg alloy.

there is a need to derive strategies that can use the interface responses without the assumption of uni-directional heat flow. Although this is often a valid assumption at the scale of dendrite growth during additive manufacturing, thermal gradients and velocities may vary by several orders of magnitude over distances as small as tens of microns.

Acknowledgements

Funding provided to PM and AP by the Natural Sciences and Engineering Council of Canada is acknowledged. Further, this manuscript has been authored by UT-Battelle, LLC under Contract No. DE-AC05-00OR22725 with the U.S. Department of Energy. Research was sponsored the U.S. Department of Energy, Office of Energy Efficiency and Renewable Energy, Advanced Manufacturing Office. The United States Government retains and the publisher, by accepting the article for publication, acknowledges that the United States Government retains a non-exclusive, paid-up, irrevocable, world-wide license to publish or reproduce the published form of this manuscript, or allow others to do so, for United States Government purposes. The Department of Energy will provide public access to these results of federally sponsored research in accordance with

the DOE Public Access Plan (http://energy.gov/downloads/doe-public-access-plan).

References

[1] T. DebRoy, H. Wei, J. Zuback, T. Mukherjee, J. Elmer, J. Milewski, A. Beese, A. Wilson-Heid, A. De, W. Zhang, Additive manufacturing of metallic components–process, structure and properties, Progress in Materials Science (2017).

[2] A. Hadadzadeh, B. S. Amirkhiz, J. Li, M. Mohammadi, Columnar to equiaxed transition during direct metal laser sintering of AlSi10Mg alloy: Effect of building direction, Additive Manufacturing 23 (2018) 121–131.

[3] C. L. Frederick, A. Plotkowski, M. M. Kirka, M. Haines, A. Staub, E. J. Schwalbach, D. Cullen, S. S. Babu, Geometry-induced spatial variation of microstructure evolution during selective electron beam melting of Rene-N5, Metallurgical and Materials Transactions A 49 (10) (2018) 5080–5096.

[4] M. M. Kirka, P. Nandwana, Y. Lee, R. R. Dehoff, Solidification and solid-state transformation sciences in metals additive manufacturing, Scripta Materialia 135 (2017) 130–134.

[5] R. Trivedi, W. Kurz, Morphological stability of a planar interface under rapid solidification conditions, Acta Metallurgica 34 (8) (1986) 1663–1670.

[6] W. . Kurz, B. Giovanola, R. Trivedi, Theory of microstructural development during rapid solidification, Acta Metallurgica 34 (5) (1986) 823–830.

[7] R. Trivedi, P. Magnin, W. Kurz, Theory of eutectic growth under rapid solidification conditions, Acta Metallurgica 35 (4) (1987) 971–980.

[8] W. Kurz, R. Trivedi, Banded solidification microstructures, Metallurgical and Materials Transactions A 27 (3) (1996) 625–634.

[9] J. Hunt, Steady state columnar and equiaxed growth of dendrites and eutectic, Materials science and engineering 65 (1) (1984) 75–83.

[10] M. Gäumann, C. Bezencon, P. Canalis, W. Kurz, Single-crystal laser deposition of superalloys: processing–microstructure maps, Acta Materialia 49 (6) (2001) 1051–1062.

[11] P. Gilgien, W. Kurz, Microstructure selection in binary and ternary alloys, Materials Science and Engineering: A 178 (1-2) (1994) 199–201.

[12] S. Fukumoto, W. Kurz, Solidification phase and microstructure selection maps for Fe-Cr-Ni alloys, ISIJ International 39 (12) (1999) 1270–1279.

[13] M. Pierantoni, M. Gremaud, P. Magnin, D. Stoll, W. Kurz, The coupled zone of rapidly solidified Al-Si alloys in laser treatment, Acta Metallurgica et Materialia 40 (7) (1992) 1637–1644.

[14] P. Gilgien, A. Zryd, W. Kurz, Microstructure selection maps for Al-Fe alloys, Acta Metallurgica et Materialia 43 (9) (1995) 3477–3487.

[15] S. Gill, W. Kurz, Rapidly solidified Al-Cu alloys II. calculation of the microstructure selection map, Acta metallurgica et materialia 43 (1) (1995) 139–151.

[16] A. Plotkowski, O. Rios, N. Sridharan, Z. Sims, K. Unocic, R. Ott, R. Dehoff, S. Babu, Evaluation of an Al-Ce alloy for laser additive manufacturing, Acta Materialia 126 (2017) 507–519.

[17] A. Plotkowski, P. Mohammadpour, A. Phillion, S. Babu, Corrigendum to "evaluation of an Al-Ce alloy for additive manufacturing"[Acta Mater. 126 (2017) 507–519], Acta Materialia (2018).

[18] J. Gockel, J. Beuth, K. Taminger, Integrated control of solidification microstructure and melt pool dimensions in electron beam wire feed additive manufacturing of Ti-6Al-4V, Additive Manufacturing 1 (2014) 119–126.

[19] N. Raghavan, R. Dehoff, S. Pannala, S. Simunovic, M. Kirka, J. Turner, N. Carlson, S. S. Babu, Numerical modeling of heat-transfer and the influence of process parameters on tailoring the grain morphology of IN718 in electron beam additive manufacturing, Acta Materialia 112 (2016) 303–314.

[20] Y.-J. Liang, X. Cheng, J. Li, H.-M. Wang, Microstructural control during laser additive manufacturing of single-crystal nickel-base superalloys: New processing–microstructure maps involving powder feeding, Materials & Design 130 (2017) 197–207.

[21] M. Haines, A. Plotkowski, C. Frederick, E. Schwalbach, S. S. Babu, A sensitivity analysis of the columnar-to-equiaxed transition for Ni-based superalloys in electron beam additive manufacturing, Computational Materials Science 155 (2018) 340–349.

[22] R. R. Dehoff, M. Kirka, W. Sames, H. Bilheux, A. Tremsin, L. Lowe, S. Babu, Site specific control of crystallographic grain orientation through electron beam additive manufacturing, Materials Science and Technology 31 (8) (2015) 931–938.

[23] M. Aziz, Model for solute redistribution during rapid solidification, Journal of Applied Physics 53 (2) (1982) 1158–1168.

[24] M. J. Aziz, T. Kaplan, Continuous growth model for interface motion during alloy solidification, Acta Metallurgica 36 (8) (1988) 2335–2347.

[25] R. Trivedi, W. Kurz, Dendritic growth, International Materials Reviews 39 (2) (1994) 49–74.

[26] G. Ivantsov, The temperature field around a spherical, cylindrical, or pointed crystal growing in a cooling solution, in: Dokl. Akad. Nauk SSSR, Vol. 58, 1947, pp. 567–569.

[27] D. Barry, J.-Y. Parlange, L. Li, Approximation for the exponential integral (Theis well function), Journal of Hydrology 227 (1-4) (2000) 287–291.

[28] J. A. Dantzig, M. Rappaz, Solidification, 1st Edition, EPFL Press, Lausanne, 2009.

[29] J. Langer, J. Müller-Krumbhaar, Stability effects in dendritic crystal growth, Journal of Crystal Growth 42 (1977) 11–14.

[30] J. Ramirez, C. Beckermann, Examination of binary alloy free dendritic growth theories with a phase-field model, Acta Materialia 53 (6) (2005) 1721–1736.

[31] T. Haxhimali, A. Karma, F. Gonzales, M. Rappaz, Orientation selection in dendritic evolution, Nature materials 5 (8) (2006) 660.

[32] W. Kurz, R. Trivedi, Eutectic growth under rapid solidification conditions, Metallurgical Transactions A 22 (12) (1991) 3051–3057.

[33] M. Lima, W. Kurz, Massive transformation and absolute stability, Metallurgical and Materials Transactions A 33 (8) (2002) 2337–2345.

[34] W. Kurz, C. Bezencon, M. Gäumann, Columnar to equiaxed transition in solidification processing, Science and Technology of Advanced Materials 2 (1) (2001) 185.

[35] W. Kurz, D. J. Fisher, Fundamentals of solidification, Vol. 1, Trans Tech Publications Aedermannsdorf, Switzerland, 1986.

[36] J. Hoyt, M. Asta, T. Haxhimali, A. Karma, R. Napolitano, R. Trivedi, B. B. Laird, J. R. Morris, Crystal–melt interfaces and solidification morphologies in metals and alloys, MRS Bulletin 29 (12) (2004) 935–939.

[37] M. Rappaz, S. David, J. Vitek, L. Boatner, Analysis of solidification microstructures in Fe-Ni-Cr single-crystal welds, Metallurgical Transactions A 21 (6) (1990) 1767–1782.

[38] D. Rosenthal, Mathematical theory of heat distribution during welding and cutting, Weld J 20 (5) (1941) 34–220.

[39] L. Thijs, K. Kempen, J.-P. Kruth, J. Van Humbeeck, Fine-structured aluminium products with controllable texture by selective laser melting of pre-alloyed AlSi10Mg powder, Acta Materialia 61 (5) (2013) 1809–1819.

[40] H. Nguyen-Thi, G. Reinhart, N. Mangelinck-Noël, H. Jung, B. Billia, T. Schenk, J. Gastaldi, J. Härtwig, J. Baruchel, In-situ and real-time investigation of columnar-to-equiaxed transition in metallic alloy, Metallurgical and Materials Transactions A 38 (7) (2007) 1458–1464.

[41] A. E. Ares, S. F. Gueijman, C. E. Schvezov, An experimental investigation of the columnar-to-equiaxed grain transition in aluminum–copper hypoeutectic and eutectic alloys, Journal of crystal Growth 312 (14) (2010) 2154–2170.

[42] H. Dong, P. D. Lee, Simulation of the columnar-to-equiaxed transition in directionally solidified Al-Cu alloys, Acta Materialia 53 (3) (2005) 659–668.

[43] X. Liu, C. Zhao, X. Zhou, Z. Shen, W. Liu, Microstructure of selective laser melted AlSi10Mg alloy, Materials & Design 168 (2019) 107677.

[44] W. Li, S. Li, J. Liu, A. Zhang, Y. Zhou, Q. Wei, C. Yan, Y. Shi, Effect of heat treatment on AlSi10Mg alloy fabricated by selective laser melting: Microstructure evolution, mechanical properties and fracture mechanism, Materials Science and Engineering: A 663 (2016) 116–125.

[45] N. T. Aboulkhair, N. M. Everitt, I. Ashcroft, C. Tuck, Reducing porosity in AlSi10Mg parts processed by selective laser melting, Additive Manufacturing 1 (2014) 77–86.